# Dipole Moment of Water in Highly Vibrationally Excited States: Analysis of Photofragment Quantum-Beat Spectroscopy Measurements Using a Local-Mode Hamiltonian†

**Patrice Theule,*,‡,§ John S. Muenter,|| and Andrea Callegari‡,⊥**

*Laboratoire de Chimie Physique et Moleculaire (LCPM), Ecole Polytechnique Fédérale de Lausanne (EPFL), CH-1015 Lausanne, Switzerland, and Department of Chemistry, University of Rochester, Rochester, New York 14627*

*Received: April 30, 2009; Revised Manuscript Received: September 1, 2009*

We present here the analysis of experimental Stark effect measurements made using photofragment quantum beat spectroscopy on the $|4,0^-\rangle$, $|5,0^-\rangle$, $|8,0^+\rangle$ and $|4,0^-\rangle|2\rangle$ vibrational states of $H_2O$ [Callegari, A.; et al. *Science* **2002**, *297*, 993.]. To link the measured Stark coefficients with the dipole surface, we analyze our results using a coupled anharmonic oscillator model, which takes into account the local-mode nature of higly excited OH stretching vibrations in water, and the tunneling between the two equivalent bonds. The large inertial frame tilt associated with the local-mode bond stretching results in a complex interaction between rotational-, vibrational-, and tunneling-motion, all of which become deeply entangled in the Stark coefficients. A perturbational approach makes it possible to analyze the problem at increasingly higher levels of approximation and to disentangle the different contributions, according to the different time scales involved. This simple model reproduces most experimental values to within a few percent, even for these highly vibrationally excited levels, and gives valuable insight into the complex rotational and vibrational motions that link the dipole moment surface with the Stark coefficients.

## I. Introduction

The dipole moment surface (DMS) of a molecule (i.e., the functional relation between the atomic coordinates and the electric dipole moment of the molecule) is a property of great practical and fundamental importance. It is, in most cases, the electric dipole that mediates energy transfer between a molecule and its environment, be it through radiative or collisional processes. This importance is reflected by the extensive amount of past and recent work aimed at accurate determinations of molecular DMS's, and by the sophisticated techniques employed for the purpose. Experiment and theory have played a complementary part in this endeavor, with, on one side, measurements of dipole moments and of absolute spectral intensities providing an accurate (if limited) sampling of the actual molecular DMS and, on the other side, ab initio and semiempirical calculations extending this information to a global DMS.

Of the two experimental approaches mentioned, dipole moment measurements (via the Stark effect) are far superior to absolute intensity measurements, in terms of accuracy and insensitivity to sample conditions, and they also bear a more straightforward relationship with the DMS. So far, however, they have been mostly limited to molecules in low energy vibrational states (typically, ground and first excited states) by the huge practical difficulties associated with first preparing highly excited vibrational states and then determining with high accuracy the small splittings induced by the interaction of the molecular dipole with an external electric field. Yet, measurements at high energies are essential for probing regions of the DMS far from the equilibrium position, which are most relevant to chemical reactions and energy transfer processes, as well as most difficult to calculate accurately from first principles.

Water is a striking example of this difficult state of affairs, its DMS being at the same time the object of great interest and the source of great challenges. The DMS for the ground electronic state of water is used to model the absorption spectrum from the microwave through the near-UV portions of the spectrum. Hence, an accurate DMS is essential for a quantitative understanding of the radiative energy transfer in the Earth's atmosphere where water is the main absorber of incoming solar radiation[1] and by far the most important greenhouse gas.[2] The fact that the best models cannot account for up to 30% of solar radiation incident on the Earth[3−6] stresses the importance of a quantitative understanding of the water absorption spectrum, hence the need for an accurate and reliable DMS. Of particular importance is the visible and near UV region of the spectrum, where solar radiation is at its maximum and where atmospheric water absorption is substantial, due to an exceedingly large number of weak transitions. The results of both direct intensity measurements and ab initio calculations in this region carry a larger uncertainty, first because they require difficult, long-path experiments (see ref 7 and references therein), and second because dipole moments and energies exhibit different convergence properties.[8−10]

Permanent dipole moments from spectroscopic measurements of the Stark effect are an ideal benchmark for DMS data, since Stark coefficients do not depend on sample conditions and can be measured with accuracies better than 0.1%.[11] Indeed, the combination of ground state and low lying excited state moments of water[12−14] has been used to improve the water DMS for geometries near equilibrium.[15] These measurements have utilized radio frequency transitions

† Part of the "Robert W. Field Festschrift".

* Corresponding author. E-mail: patrice.theule@univ-provence.fr.

‡ Ecole Polytechnique Fédérale de Lausanne (EPFL).

§ Also at: Physique des Interactions Ioniques et Moléculaires, UMR 6633, Université de Provence et CNRS, Centre de Saint-Jérôme, 13397 Marseille cedex 20, France.

|| University of Rochester.

⊥ Current address: SICPA Management SA, Av. de Florissant 41, 1008 Prilly, Switzerland.

10.1021/jp904035g CCC: $40.75 © 2009 American Chemical Society
Published on Web 10/29/2009

between Stark components, within individual rotational levels.[12,13] However, extending Stark effect measurements to higher energy states (accessed by vibration−rotation transitions) is difficult because Doppler widths of infrared and visible transitions are typically larger than Stark splittings. In water, the task is further complicated by very small Stark coefficients and by rotational transitions falling in the submillimeter spectral region.

To measure Stark coefficients in highly vibrationally excited states of water, we have turned to a different approach using a combination of multiple-laser vibrational overtone spectroscopy, photofragment detection and electric field induced quantum beats.[16−19] This method is the time-domain analog of radio frequency, electric resonance experiments.[20] The quantum beats (arising from the electric field induced splittings of the $M$ sublevels) provide an excellent way to measure the Stark effect and, hence, dipole moments, and this method has been applied in a variety of experiments.[16,18,19,21−24]

A brief report of the $H_2O$ work has appeared in Science,[16] and a complete description of this method for Stark effect measurements has been presented in our discussion of excited state dipole moment measurements in the HDO isotopic variant of water.[19]

The detailed analysis of the HDO results was published first because linking the measured Stark coefficients with the permanent dipole moment of the molecule is a much more straightforward task for this isotopomer. Specifically, in HDO the two bonds are mechanically inequivalent, because of the significant mass difference between H and D; hence, the overtone excitation is effectively localized in one bond (OH, in our case) and the excited molecule is well described by a conventional rotation-vibration Hamiltonian. In $H_2O$, instead, tunneling between the two identical OH bonds complicates the picture substantially and requires a careful analysis of the combined effect of vibrations, rotations, and tunneling.

We present here a detailed analysis of the $H_2O$ measurements, using a simple yet very insightful semiempirical model of water's highly excited vibrational modes. This model accounts for the interaction between vibrational motion, molecular rotation, and the tunneling of vibrational energy between identical O−H bonds, and it takes advantage of the fact that these motions occur on quite different time scales to disentangle their effects. Proper analysis must average different molecular properties over their appropriate time scales to obtain both correct results and useful insight. While the numerical implementation of this model is fairly elaborate, the fact that the process can be presented as a series of progressively higher order perturbations makes the overall process quite intuitive.

The paper is organized as follows. Section II briefly outlines the experimental considerations discussed in ref 19, and presents the experimental results. Section III provides details of the data analysis, including a brief discussion of local mode splitting and dipole moment matrix elements between local mode states. Experimentally observed Stark coefficients are then compared with those obtained from our semiempirical model. We conclude in section IV with a discussion of the results obtained.

## II. Experiment and Results

A detailed description of the experimental setup is given in our HDO paper.[19] Briefly, we use nanosecond pulsed lasers to excite O−H stretching overtones, to dissociate the vibrationally excited water molecules, and to detect the resulting OH radical fragments, as outlined schematically in Figure 1. The vibrational states studied here are labeled as $|4,0^-\rangle$, $|5,0^-\rangle$, $|8,0^+\rangle$, and $|4,0^-\rangle|2\rangle$, according to a widespread notation.[25] The first three contain, respectively, 4, 5, and 8 quanta of OH stretching vibration in a symmetric (+) or antisymmetric (−) combination of local modes; the last contains, in addition to 4 quanta of OH stretching, also 2 quanta of bending.[26] This notation is explained in detail in the DATA ANALYSIS section.

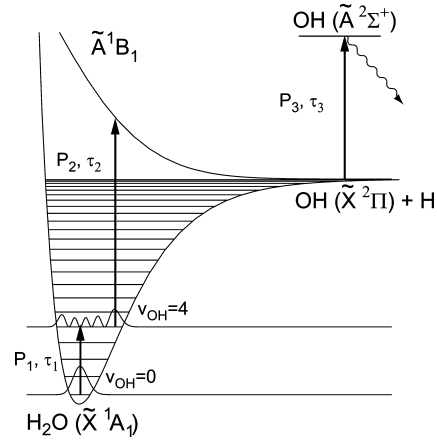


**Figure 1.** Schematic of the relevant potential energy surfaces, energy levels, transitions, and laser pulses used for the measurement of Stark induced quantum beats in water.

The $|8,0^+\rangle$ state was populated through the $|4,0^-\rangle$ state with two sequential laser pulses, $P_{1a}$ and $P_{1b}$, separated by a short delay (~10 ns).[19,27] The specific laser configurations used to study the $|4,0^-\rangle$, $|5,0^-\rangle$, and $|8,0^+\rangle$ states are the same as HDO, and they are summarized in Table 1. For the $|4,0^-\rangle|2\rangle$ state, we have used the same laser configuration as for $|5,0^-\rangle$. Details of data acquisition, electric field generation and calibration, and laser pulse delay-time measurements are also the same as used for HDO.[19]

Laser wavelengths are chosen to excite and probe a single state $|i\rangle \equiv |v,J,K_a,K_c\rangle$, with a specific set of vibrational and rotational quantum numbers. According to common notation, we indicate the vibrational quantum number with $v$, the rotational quantum number with $J_{K_a,K_c}$ (or equivalently $J_\tau$ with $\tau = K_a - K_c$ when a more compact notation is desired), and the magnetic quantum number with $M$. The rotational states investigated here are the three with $J = 1$, namely $1_{01}$, $1_{11}$, and $1_{10}$. The polarization of the first laser pulse $P_1$ is chosen to create a wave packet consisting of a coherent superposition of $|J = 1,\tau,M = 0\rangle$ and $|J = 1,\tau,M = \pm 1\rangle$ Stark components. A uniform electric field $\mathcal{E}$ of up to 5 kV/cm is used to split the degenerate $M$ sublevels, thus making the wavepacket precess around the direction of the Stark field, at a frequency of a few megahertz. All that is necessary to complete the Stark effect measurement is a means to detect the resultant quantum beats, and we use a variation of the vibrationally mediated photodissociation experiments of Crim and co-workers[28] to detect the quantum beats with high sensitivity and accurate time-resolution. The quantum yield, $\Phi$, for photodissociation caused by laser pulse $P_2$ depends on (i) the time delay between laser pulses $P_1$ and $P_2$, $\Delta t = t_2 - t_1$, (ii) the precession frequency, $f_{QB}$, and (iii) laser polarizations and the symmetry properties of the $\tilde{A} \leftarrow X$ electronic transition.[29] To probe the quantum yield, a third laser pulse, $P_3$, excites the OH fragments, and a photomultiplier detects the resulting laser induced fluorescence (LIF), giving a signal $S$, proportional to $\Phi$:

$$S = k_1[1 + k_2 \cos(2\pi f_{QB}\Delta t + \varphi)] \quad (1)$$

**TABLE 1: Summary of the Molecular Transitions, and of the Laser Configurations Used To Measure the Stark Coefficient of Highly Excited Vibrational States of Water[a]**

| pump<br>$H_2O$, $\tilde{X}^1A_1 \rightarrow \tilde{X}^1A_1$ | dissociation<br>$H_2O$, $\tilde{X}^1A_1 \rightarrow \tilde{A}^1B_1$ | probe<br>OH, $\tilde{X}^2\Pi \rightarrow \tilde{A}^2\Sigma^+$ |
|---|---|---|
| $\mathbf{P_1}$ (45°): $\|00\rangle \rightarrow \|40^-\rangle$<br>$0_{00} \rightarrow 1_{01}$, 13853.27 $cm^{-1}$<br>$1_{10} \rightarrow 1_{11}$, 13821.91 $cm^{-1}$<br>$1_{11} \rightarrow 1_{10}$, 13832.25 $cm^{-1}$ | $\mathbf{P_2}$ (45°)<br>37576 $cm^{-1}$ | $\mathbf{P_3}$ (0°)<br>$Q_1(1)$, 32474.58 $cm^{-1}$ |
| $\mathbf{P_1}$ (45°): $\|00\rangle \rightarrow \|40^-2\rangle$<br>$0_{00} \rightarrow 1_{01}$, 16844.01 $cm^{-1}$<br>$1_{10} \rightarrow 1_{11}$, 16816.97 $cm^{-1}$<br>$1_{11} \rightarrow 1_{10}$, 16827.88 $cm^{-1}$ | $\mathbf{P_2}$ (45°)<br>37576 $cm^{-1}$ | $\mathbf{P_3}$ (0°)<br>$Q_1(1)$, 32474.58 $cm^{-1}$ |
| $\mathbf{P_1}$ (45°): $\|00\rangle \rightarrow \|50^-\rangle$<br>$0_{00} \rightarrow 1_{01}$, 16920.94 $cm^{-1}$<br>$1_{10} \rightarrow 1_{11}$, 16889.93 $cm^{-1}$<br>$1_{11} \rightarrow 1_{10}$, 16900.26 $cm^{-1}$ | $\mathbf{P_2}$ (45°)<br>37576 $cm^{-1}$ | $\mathbf{P_3}$ (0°)<br>$Q_1(1)$, 32474.58 $cm^{-1}$ |
| $\mathbf{P_{1a}}$ (0°) + $\mathbf{P_{1b}}$ (45°): $\|00\rangle \rightarrow \|40^-\rangle \rightarrow \|80^+\rangle$<br>$1_{01} \rightarrow 0_{00} \rightarrow 1_{01}$, 13807.17 + 11309.68 $cm^{-1}$<br>$1_{11} \rightarrow 1_{10} \rightarrow 1_{11}$, 13832.25 + 11280.77 $cm^{-1}$<br>$1_{10} \rightarrow 1_{11} \rightarrow 1_{10}$, 13821.91 + 11290.37 $cm^{-1}$ | $\mathbf{P_2}$ (45°)<br>28182 $cm^{-1}$ | $\mathbf{P_3}$ (0°)<br>$Q_1(1)$, 32474.58 $cm^{-1}$ |

[a] See text for notation and details.

The Stark shifts encountered here are extremely small when compared with the separation between the relevant vibration−rotation states; hence, we observe second-order Stark splittings, proportional to $\mathcal{E}^2$. Thus the simplest form of the experimental signal, $S$, is

$$S_i(\mathcal{E},t) = k_1[1 + k_2 \cos(2\pi C_i \mathcal{E}^2 \Delta t + \varphi)] \qquad (2)$$

where $C_i$ is the second-order Stark coefficient for the specific state $|i\rangle = |v,J,K_a,K_c\rangle$ being investigated[11] and $\varphi$ is a phase factor that depends on the geometry of the experiment. Measuring $S$ as a function of either $\Delta t$ or $\mathcal{E}^2$ results in a characteristic oscillatory pattern, from which the Stark coefficient can be deduced. We find it more convenient to scan the electric field while keeping $\Delta t$ fixed to about 400 ns, which is the largest value compatible with dephasing collisions and with the transit time of molecules through the laser beams.

Figure 2 shows plots of $S$ vs $\mathcal{E}$ for each of the three $J = 1$ states of $H_2O$ containing 4 quanta of O−H stretch. Similar data have been recorded for the $|4,0^-\rangle|2\rangle$, $|5,0^-\rangle$, and $|8,0^+\rangle$ vibrational states. Superimposed on the characteristic oscillatory pattern we also observe a small systematic dependence of the overall signal amplitude on $\mathcal{E}$ for which we have not, at present, found a completely satisfactory explanation.

Accordingly, we fit the experimental data to a more general form of eq 2:

$$S_i(\mathcal{E}) = k_1(1 + k_3\mathcal{E}^2)[1 + k_2 \cos(2\pi C_i \mathcal{E}^2 \Delta t + \varphi)] \qquad (3)$$

where $k_1$ scales the signal amplitude, $k_2$ specifies the quantum beat contrast, and $k_3$ describes any systematic $\mathcal{E}$-field dependence of the amplitude, $C_i$ is the desired second-order Stark coefficient, and $\varphi$ is the phase factor. In $k_1$ are lumped all the factors determining the overall signal strength (laser power, transition strengths, geometry of the experiment, photon collection efficiency, etc.). Some $J_{K_aK_c}$ states exhibit small negative values for $k_3$, as is the case for the $1_{10}$ and $1_{11}$ data in Figure 2, while other rotational levels, such as the $1_{01}$ data in Figure 2, exhibit small positive $k_3$'s.

The contrast factor, $k_2$ can vary from zero to one[29] and the high contrast we observe arises from a careful choice of the chain of transitions leading to the fluorescence of the OH fragment.[17,19] The phase angle, $\varphi$, depends on laser polarizations and on the transitions used in the experiment, and it is close to an integer multiple of $\pi$, as can be seen by comparing the three curves in Figure 2. From the fit, we obtain the Stark coefficient

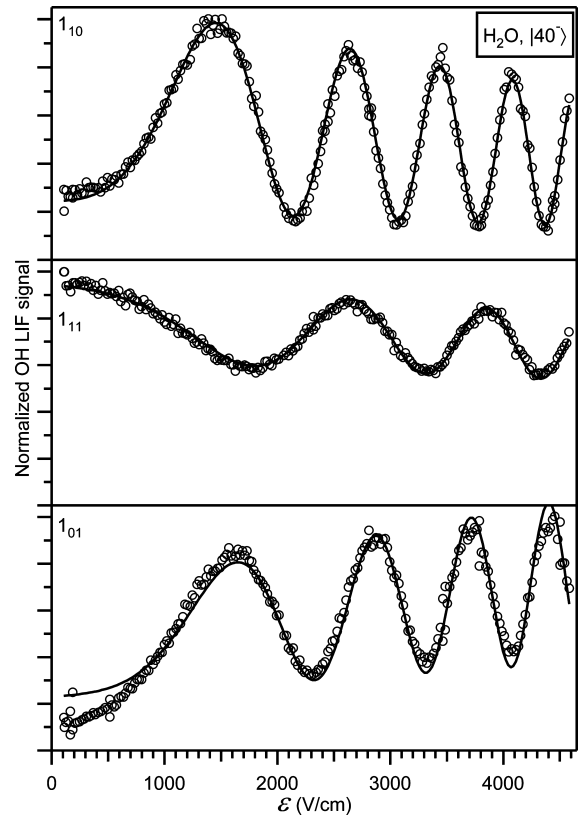


**Figure 2.** Normalized quantum beats signal for the $1_{10}$, $1_{11}$, and $1_{01}$ rotational states of the $|4,0^-\rangle$ vibrational state of $H_2O$. The horizontal line at the bottom of each panel corresponds to the zero baseline.

**TABLE 2: Experimental Stark Coefficients for Different Rotation−Vibration States of $H_2O$[a]**

| $J_{K_aK_c}$ | $\|4,0^-\rangle$ | $\|4,0^-\rangle\|2\rangle$ | $\|5,0^-\rangle$ | $\|8,0^+\rangle$ |
|---|---|---|---|---|
| $1_{01}$ | 0.4372(8) | 0.3153(26) | 0.4277(7) | 0.4953(16) |
| $1_{11}$ | 0.3160(9) | 0.2137(39) | 0.3032(7) | 0.4250(10) |
| $1_{10}$ | 0.5097(10) | 0.6306(27) | 0.5077(4) | 0.6657(38) |

[a] Units are (Hz cm$^2$ V$^{-2}$), and 1$\sigma$ uncertainties on the last digit are given in parentheses.

$C_i$ for each vibration−rotation state, and the solid lines in Figure 2 show the fits for the displayed data. There are no significant correlations among the fitted parameters; the resulting $C_i$'s and their standard deviations are reported in Table 2.

## III. Data Analysis

All of the fundamental information provided by Stark measurements is contained in the $C_i$ coefficients. Their relation to dipole moments is summarized in eq 4 for a generic state $|i\rangle$, with energy $E_i$: the second-order Stark effect depends on the electric field induced interactions of $|i\rangle = |v, J, K_a, K_c\rangle$ with all possible states $|j\rangle = |v',J',K'_a,K'_c\rangle$ through dipole moment matrix elements, $\mu_{ij}$.[11]

$$\Delta E_i = \sum_{j\neq i} \frac{\mu_{ij}^{\ 2}\mathcal{E}^2}{E_i - E_j} \equiv hC_i\mathcal{E}^2 \tag{4}$$

Formally, the most straightforward method to compare the results of experimental measurements with ab initio calculations is to compute Stark coefficients using the calculated dipole moment matrix elements and either the calculated or the experimental energy levels, whichever are more accurate (generally, the latter, when available). While being the most accurate for comparison, this approach provides little physical insight on the relation between vibrational motion, dipole surface, and Stark coefficients; in particular, it does not provide an intuitive picture of the evolution of the molecular charge distribution with vibrational excitation. Traditionally, Stark coefficients are used to derive a well-defined dipole moment, associated with each vibrational state.[13,14] Then, the magnitude and orientation of molecular electric dipole moments provide a much more accessible and insightful descriptions of vibrationally induced changes in the electronic structures of molecules. This treatment implicitly requires that rotational and vibrational motions can be separated, i.e., that the wave function can be written as the product of a rotational and a vibrational term, $|i\rangle = |v\rangle|J,K_a,K_c\rangle$. When this is the case, only angular coordinates need to be explicitly considered in calculating the $\mu_{ij}$ matrix elements, and the vibrational state dependence remains incorporated in permanent moment dipole matrix elements $\langle v|\mu|v\rangle \equiv \langle\mu\rangle_v$. The contribution from transition dipole matrix elements of the type $\langle v'|\mu|v\rangle$ with $v \neq v'$ is usually discarded as negligible, on account of the smallness of the matrix elements and of the large energy separation between vibrational states. Then, the relevant dipole moment matrix elements are written in the general form:

$$\mu_{ij} = \sum_{g=a,b,c} \langle\mu_g\rangle_v \phi^g_{J\tau MJ'\tau'M} \tag{5}$$

where $\langle\mu_g\rangle_v$ is the projection of the vibrationally averaged dipole moment on the $g$th principal axis of inertia ($g = a, b, c$) and the $\phi^g_{J\tau MJ'\tau'M}$ are direction cosine matrix elements.[11] Notice that rigid-rotor selection rules prescribe that for a given set of rotational quantum numbers $\{J, K_a, K_c, J', K'_a, K'_c\}$ at most one of the three components $\mu_a$, $\mu_b$, $\mu_c$ contributes to the corresponding $\mu_{ij}$.

The Stark effect described in eq 4 is now written in terms of vibrationally averaged dipole moment components along each of the inertial axes,

$$\Delta E_i = \sum_{\substack{J'\tau'\neq J\tau \\ g=a,b,c}} \frac{(\langle\mu_g\rangle_v \phi^g_{J\tau MJ'\tau'M})^2\mathcal{E}^2}{E_{J\tau} - E_{J'\tau'}} \equiv hC_i\mathcal{E}^2 \tag{6}$$

which, given at least three Stark coefficients $C_i$, allows one to determine the three averaged dipole components from the observed Stark coefficients (in water, $\mu_c$ is identically zero, on account of planar symmetry, and two Stark coefficients would suffice). For HDO this approach has produced accurate values for the $\langle\mu_a\rangle_v$ and $\langle\mu_b\rangle_v$ components of the dipole moment in several high energy states.[19] We have then used these values to develop and validate a one-dimensional model of the dipole moment, which describes in detail both the mechanical and the electronic contribution to the vibrational dependence of the observed dipole moment components.[19] Unfortunately, this separation of vibrational and rotational motion cannot be carried out in the same straightforward fashion when large-amplitude vibrational motion, such as tunneling, is present. This is the case for $H_2O$ in highly vibrationally excited O−H stretching states, where large-amplitude tunneling motion occurs between the two equivalent O−H bonds. However, the separation can be recovered by considering first a zero-order approximation of the water molecule with uncoupled OH stretching vibrations, and then reintroducing coupling stepwise in increasingly higher orders of approximation (corresponding to first- and second-order perturbation theory). Water lends itself well to this treatment because highly excited OH stretching vibrations are only weakly coupled across the two bonds. In fact, water vibrational states with several quanta in OH stretching modes are best described as symmetric/antisymmetric combinations of local modes,[27,30,31] i.e., of modes where the stretching excitation is localized in one or the other of the two identical O−H bonds.

Common notation[25] specifies the number of quanta of vibration in each identical O−H oscillator in the uncoupled picture as $|m,n\rangle$, meaning $m$ quanta of O−H stretch in bond 1 and $n$ quanta in bond 2. In the absence of coupling, this state is degenerate with its counterpart $|n,m\rangle$.

All of the states studied here have only one of the O−H bonds excited, in the local picture, corresponding to the two local mode oscillators, $|n,0\rangle$ and $|0,n\rangle$. Once coupling is introduced, the interaction between the degenerate $|n,0\rangle$ and $|0,n\rangle$ states removes the degeneracy and the resulting eigenstates are the symmetric and antisymmetric linear combinations:

$$|n,0^+\rangle \equiv (|n,0\rangle + |0,n\rangle)/\sqrt{2} \tag{7a}$$

$$|n,0^-\rangle \equiv (|n,0\rangle - |0,n\rangle)/\sqrt{2} \tag{7b}$$

To complete the above picture, when bending excitation is also present, the number of bending quanta, $|b\rangle$, is appended to the stretching notation, $|n,m^{\pm}\rangle|b\rangle$.

Much has been written about the local mode representation, and several criteria exist for judging the transition from normal

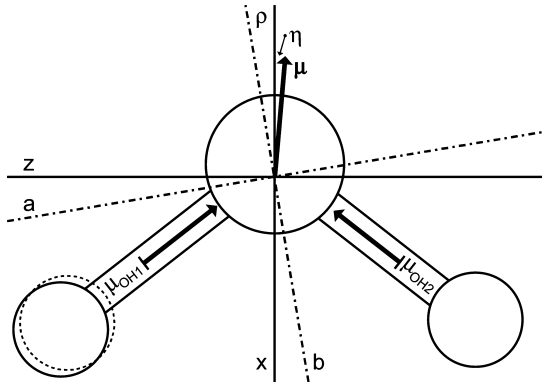


**Figure 3.** Schematic of the changes that occur in $H_2O$ upon OH bond stretching that are relevant to dipole moment analyses. The inertial frame $a-b$ tilts away from the $C_{2v}$ frame $z-x$ by an angle $\rho$, due to the displacement of nuclear mass. The electric dipole moment vector $\mu$ changes in magnitude *and* direction, rotating by an angle $\eta$, due to the displacement of nuclear charge and redistribution of electronic charge.

to local mode behavior.[25,30,31] One of the simplest is the magnitude of the splitting between pairs of states, $E(|n,0^-\rangle) - E(|n,0^+\rangle)$. Small splittings indicate highly localized vibrations, and the $H_2O$ states studied in this work have $E(|4,0^-\rangle) - E(|4,0^+\rangle) \approx 2.7$ cm$^{-1}$, $E(|5,0^-\rangle) - E(|5,0^+\rangle) \approx 0.4$ cm$^{-1}$,[32,33] $E(|4,0^-\rangle|2\rangle) - E(|4,0^+\rangle|2\rangle) \approx 0.2$ cm$^{-1}$, and $E(|8,0^-\rangle) - E(|8,0^+\rangle) \simeq 0.0$ cm$^{-1}$ as experimentally measured.[34]

The $E(|n,0^-\rangle) - E(|n,0^+\rangle)$ splitting results from the coupling-induced tunneling between the two local-mode basis states, and the rapid decrease in the separation between the + and − states with increasing $n$ reflects the difficulty of transferring larger number of quanta from one O−H bond to the other. In the harmonically coupled, anharmonic oscillator model of local modes,[31] the matrix element responsible for the tunneling between $|n,0\rangle$ and $|0,n\rangle$ is of order $n$, so a larger $n$ corresponds to a higher order interaction and hence a smaller splitting between the $|n,0^{\pm}\rangle$ states.

For any process occurring on a time scale which is fast relative to the tunneling between the $|n,0\rangle$ and the $|0,n\rangle$ states, water is well described (in a zero-order approximation) as an asymmetric molecule having only one O−H bond excited. Since the splittings in the vibrational states studied here are small relative to rotational spacings, rotational motion is faster than tunneling and it is appropriate to start with the zero-order approximation and use the $|n,0\rangle$ and $|0,n\rangle$ basis functions to describe the rotational properties of this asymmetric water molecule, including the Stark effect. The necessary symmetry of the wave functions will be introduced later on, following a perturbative approach.

**A. Zero-Order Approximation.** We begin the zero-order analysis by temporarily neglecting tunneling and consider just the $|n,0\rangle$ local-mode state, thus treating the two bonds as inequivalent. Without tunneling, it is appropriate to treat this state in the usual semirigid rotor approach, as we did for HDO, and factor out rotational and vibrational wave functions. Anharmonicity causes the excited bond to have a longer vibrationally averaged length, which results in two major effects. First, the resulting asymmetric mass distribution tilts the inertial frame away from the $C_{2v}$ frame appropriate for the ground state by an angle $\rho$, as shown schematically in Figure 3. Second, the bond elongation alters the molecular charge distribution, producing a change in the magnitude and direction of the molecular dipole moment vector, which rotates by an angle $\eta$ away from the original $C_2$ axis. Both the frame rotation and the charge redistribution thus affect the projections of the molecular dipole on the new inertial axes. A third, less dramatic effect that must be considered is that the bond angle also changes slightly upon O−H excitation. The situation is conceptually analogous to what we observed for HDO, but the initial orientation of the inertial axes and their subsequent rotation are substantially different in the two cases. In the case of $H_2O$, the $b$-axis is initially aligned with the bisectrix of the HOH angle, and moves away from it as the OH bond is stretched, while for HDO the situation is reversed.

To get a sense of the relative sizes of $\rho$ and $\eta$, consider a simple bond moment model that fixes the bond lengths, $R_1$ and $R_2$, the two bond moments, $\mu_1$ and $\mu_2$, and the bond angle, $\theta$, at realistic values for the $|4,0^-\rangle$ state. $R_2 = 0.972$ Å and $\mu_2 = 1.515$ D are taken from the ground state, appropriate for the unexcited bond. The $A$ and $B$ rotational constants for the $|4,0\rangle$ state then give $R_1 = 1.015$ Å and a bond angle of $\theta = 102.9°$. This geometry and $\mu_2$, plus a typical linear dipole moment function of 1 D/Å for the OH bond, gives $\mu_1 = 1.558$ D. These estimates produce $\rho = -4.2°$, $\mu_{\text{total}} = 1.92$ D, $\eta = 1.0°$, and thus $\mu_a = 0.17$ D, $\mu_b = 1.91$ D, with the orientation of the $a-b$ inertial frame and the definitions of $\rho$ and $\eta$ as shown in Figure 3. This rough estimation, which is rather close to what we observe, shows that a quite substantial change in the $\mu_a$ dipole moment component is expected, primarily from the inertial frame rotating away from the $C_{2v}$ axes.

**B. First-Order Approximation.** In the zero-order picture, we have purposefully neglected tunneling, and this has allowed us to treat each local mode as independent and the two bonds as inequivalent, since only one of them is excited. A rigorous treatment of water rotational−vibrational motion must include tunneling, which re-establishes the equivalence of the two bonds and, hence, requires that the wave functions be properly symmetrized with respect to the permutation symmetry of the Hamiltonian. This is done by introducing a coupling term, $\lambda$, in the local-mode Hamiltonian. Following Lehmann,[35] we write

$$\begin{aligned}\mathbf{H} = {} & [G_0 + A\hat{J}_{a1}^{\,2} + B\hat{J}_{b1}^{\,2} + C\hat{J}_{a1}^{\,2}]|1\rangle\langle 1| + \\ & [G_0 + A\hat{J}_{a2}^{\,2} + B\hat{J}_{b2}^{\,2} + C\hat{J}_{a2}^{\,2}]|2\rangle\langle 2| + \\ & \lambda[|2\rangle\langle 2| + |1\rangle\langle 1|]\end{aligned} \quad (8)$$

In this expression $G_0$ is the vibrational energy of the local-mode basis states, $|1\rangle \equiv |n,0\rangle$ and $|2\rangle \equiv |0,n\rangle$, and $\lambda$ describes the interaction that removes the degeneracy between these states. The $\hat{J}_{g_1}$ and $\hat{J}_{g_2}$ ($g_i = a_i, b_i, c_i$) angular momentum operators are defined in the inertial coordinate systems of the $|1\rangle$ and $|2\rangle$ basis states, respectively. The rotational constants in the $\{a_1, b_1, c_1\}$ and $\{a_2, b_2, c_2\}$ coordinate systems are equal to one another by symmetry and the two coordinate systems are mirror images, rotated by an angle $\rho$ in opposite directions from the $C_{2v}$ axis system of the equilibrium structure. Accordingly, each coordinate system has a set of rotational wave functions, $|J,\tau\rangle_1$ and $|J,\tau\rangle_2$, that diagonalize the rotational Hamiltonian of the corresponding local mode, giving energies $E_{J,\tau}^{(1)} = E_{J,\tau}^{(2)} \equiv E_{J,\tau}^{\text{loc}}$; the two sets are identical but referred to different quantization axes. It is important to remark that rotational wave functions referred to different quantization axes do not obey the usual orthogonality relationships; hence the last term in eq 8 also couples local modes with different $\tau$ rotational quantum number. Wave functions with different values of $J$, on the other hand, are not coupled, since they remain orthogonal to one another.

In first-order perturbation, we need to consider only coupling between degenerate states ($\tau = \tau'$), which corresponds to taking the limit where tunneling is much slower than rotational motion (i.e., $\lambda$ much smaller than the spacing between rotational levels). Furthermore, as long as $\rho$ is small, the coupling between these degenerate states is not modified by the frame rotation. Hence, at this stage, this lack of orthogonality can be neglected, and the symmetrized eigenstates are simply given by

$$|+,J,\tau\rangle \equiv \frac{|1\rangle|J,\tau\rangle_1 + |2\rangle|J,\tau\rangle_2}{\sqrt{2}} \tag{9a}$$

$$|-,J,\tau\rangle \equiv \frac{|1\rangle|J,\tau\rangle_1 - |2\rangle|J,\tau\rangle_2}{\sqrt{2}} \tag{9b}$$

with energies $E^+_{J,\tau} = E^{\mathrm{loc}}_{J,\tau} + \lambda$ and $E^-_{J,\tau} = E^{\mathrm{loc}}_{J,\tau} - \lambda$. Notice that for these eigenstates it is no longer possible to separate vibrations and rotations (i.e., write the eigenstate as the product of one vibrational and one rotational wave function) as is normally done for a semirigid rotor.

The relevant dipole moment matrix elements are the two permanent dipole matrix elements:

$$\begin{aligned}
&\mu^{\pm\pm}_{J,\tau,M,J',\tau',M} \\
&= \frac{1}{2}[(\langle J,\tau,M|_1\langle 1| \pm \langle J,\tau,M|_2\langle 2|)\mu(|1\rangle|J',\tau',M\rangle_1 \pm |2\rangle|J',\tau',M\rangle_2)] \\
&= \frac{1}{2}[(\langle J,\tau,M|_1\langle 1|\mu|1\rangle|J',\tau',M'\rangle_1 + \langle J,\tau,M|_2\langle 2|\mu|2\rangle|J',\tau',M'\rangle_2)] \\
&= \frac{1}{2}[(\langle\mu_a\rangle_1\phi^a_{J\tau MJ'\tau'M} + \langle\mu_b\rangle_1\phi^b_{J\tau MJ'\tau'M} + \langle\mu_a\rangle_2\phi^a_{J\tau MJ'\tau'M} + \\
&\qquad \langle\mu_b\rangle_2\phi^b_{J\tau MJ'\tau'M})] \\
&= \langle\mu_b\rangle\phi^b_{J\tau MJ'\tau'M}
\end{aligned} \tag{10a}$$

and the two transition dipole moments

$$\begin{aligned}
&\mu^{\pm\mp}_{J,\tau,M,J',\tau',M} \\
&= \frac{1}{2}[(\langle J\tau M|_1\langle 1| \pm \langle J\tau M|_2\langle 2|)\mu(|1\rangle|J'\tau'M\rangle_1 \mp |2\rangle|J'\tau'M\rangle_2)] \\
&= \frac{1}{2}[(\langle J\tau M|_1\langle 1|\mu|1\rangle|J'\tau'M\rangle_1 - \langle J\tau M|_2\langle 2|\mu|2\rangle|J'\tau'M\rangle_2)] \\
&= \frac{1}{2}(\langle\mu_a\rangle_1\phi^a_{J\tau MJ'\tau'M} + \langle\mu_b\rangle_1\phi^b_{J\tau MJ'\tau'M} - \langle\mu_a\rangle_2\phi^a_{J\tau MJ'\tau'M} - \\
&\qquad \langle\mu_b\rangle_2\phi^b_{J\tau MJ'\tau'M}) \\
&= \langle\mu_a\rangle\phi^a_{J\tau MJ'\tau'M}
\end{aligned} \tag{10b}$$

Notice that the second equalities in eqs 10a and 10b discard matrix elements between the $|1\rangle$ and $|2\rangle$ states, such as $\langle J\tau M|_1\langle 1|\mu|2\rangle|J'\tau'M\rangle_2$, because these terms are negligibly small compared to the matrix elements retained, since $\langle J\tau M|_1\langle 1|\mu|2\rangle|J'\tau'M\rangle_2$, is of the same order as the transition moment for an $n$th overtone, as discussed above. The third equalities in eqs 10 separate the vibrationally averaged dipole moment from the rotational coordinates and write the vector $\langle\mu\rangle_v$ in terms of its projections on the $a$ and $b$ inertial axes, $\langle\mu_a\rangle_v$ and $\langle\mu_b\rangle_v$, times direction cosine matrix elements. The final equalities, and significant simplifications of eqs 10, arise from symmetry requiring that $\langle\mu_a\rangle_1 = -\langle\mu_a\rangle_2 \equiv \langle\mu_a\rangle$ and $\langle\mu_b\rangle_1 = \langle\mu_b\rangle_2 \equiv \langle\mu_b\rangle$

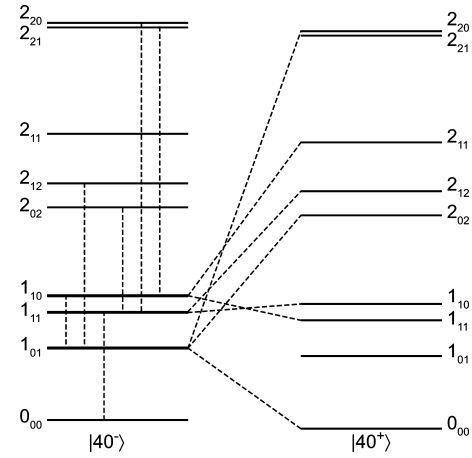


**Figure 4.** Water rotation−vibration energy levels for the $|4,0^{\pm}\rangle$ eigenstates. The dashed lines represent dipole moment matrix elements connecting the $J = 1$ states with the other relevant ro-vibrational states. Vertical lines represent $b$-type matrix elements, while diagonal lines $a$-type matrix elements.

Equation 10a states that the $b$ component of the dipole moment in the local-mode basis becomes the permanent dipole moment of the symmetrized basis state, while eq 10b shows that the $a$ component of the (permanent) local-mode moment becomes a transition dipole connecting the $|+\rangle$ and $|-\rangle$ symmetrized eigenstates. This situation is quite analogous to the Stark effect observed in ammonia, which arises from transition moments connecting the two halves of the tunneling doublets of $NH_3$.[11] This transition moment is conventionally interpreted as the permanent moment of $NH_3$ in the pyramidal geometry of either the left- or right-handed basis state. Inversion of the pyramidal basis states changes the sign of the $NH_3$ moment, just as tunneling from $|n,0\rangle$ to $|0,n\rangle$ reverses the sign of $\mu_a$ in the local-mode description of water. In both cases, permanent moments in local basis states become transition moments between the eigenstates when tunneling becomes feasible.

The specific dipole moment matrix elements, $\mu_{ij}$, required to analyze $J = 1$ Stark effects are shown schematically in Figure 4, which uses the $|4,0^{\pm}\rangle$ states as an example. The $b$-type matrix elements are shown as vertical dashed lines within the $|4,0^-\rangle$ manifold, while the $a$-type matrix elements appear as diagonal lines connecting the two manifolds of $|4,0^{\pm}\rangle$ eigenstates. The observed Stark coefficients are quite sensitive to even relatively small $a$-type dipole moment matrix elements because of the close proximity of the two pairs of states: $|4,0^+\rangle|1_{10}\rangle$, $|4,0^-\rangle|1_{11}\rangle$, and $|4,0^+\rangle|1_{11}\rangle$, $|4,0^-\rangle|1_{10}\rangle$.

**C. Second-Order Correction.** In the limit of vanishingly small $\lambda$ considered so far, each matrix element represented by a vertical dashed line in Figure 4 has contributions from only $\langle\mu_b\rangle_v$, while the matrix elements represented by diagonal dashed lines depend only on $\langle\mu_a\rangle_v$. However, when $\lambda$ is finite, a non-negligible mixing arises from the off-diagonal coupling described in eq 8.

$$V^{\pm\pm}_{J\tau J'\tau'} = \langle\pm,J,\tau|\mathbf{H}|\pm,J',\tau'\rangle = \pm\delta_{JJ'}\frac{\lambda}{2}[\langle J,\tau|_2 J',\tau'\rangle_1 + \langle J,\tau|_1 J',\tau'\rangle_2] \tag{11a}$$

$$V^{\pm\mp}_{J\tau J'\tau'} = \langle \pm,J,\tau|\mathbf{H}|\pm,J',\tau'\rangle = \pm\delta_{JJ'}\frac{\lambda}{2}[\langle J,\tau|_2 J',\tau'\rangle_1 - \langle J,\tau|_1 J',\tau'\rangle_2] \quad (11b)$$

We can quantify this coupling by using the rotation operator $\exp(i\rho\hat{J}_c)$ to bring the rotational wave functions to a common set of axes:

$$V^{\pm\pm}_{J\tau J'\tau'} = \pm\delta_{JJ'}\frac{\lambda}{2}[\langle J,\tau|\exp(2i\rho\hat{J}_c)|J',\tau'\rangle + \langle J,\tau|\exp(-2i\rho\hat{J}_c)|J',\tau'\rangle] \quad (12a)$$

$$V^{\pm\mp}_{J\tau J'\tau'} = \pm\delta_{JJ'}\frac{\lambda}{2}[\langle J,\tau|\exp(2i\rho\hat{J}_c)|J',\tau'\rangle - \langle J,\tau|\exp(-2i\rho\hat{J}_c)|J',\tau'\rangle] \quad (12b)$$

For the small values of $\rho$ we have to deal with, we can write $\pm\exp(2i\rho\hat{J}_c) \approx 1 \pm 2i\rho\hat{J}_c$, and

$$V^{\pm\pm}_{J\tau J'\tau'} \approx \pm\lambda\delta_{JJ'}\delta_{\tau\tau'} \quad (13a)$$

$$V^{\pm\mp}_{J\tau J'\tau'} \approx \pm 2i\lambda\rho\delta_{JJ'}\langle J,\tau|\hat{J}_c|J',\tau'\rangle \quad (13b)$$

The first term is responsible for the first-order splitting of the degenerate $|+,J,\tau\rangle$, $|-,J,\tau\rangle$ states already discussed and accounted for. The second term, connects states *across* the $+ -$ manifolds, whose rotational quantum numbers satisfy $J = J'$, $K_a = K'_a \pm 1$, and $K_c = K'_c$ and results in a partial scrambling of the ro-vibrational wave functions:

$$|(+,J,\tau)\rangle \approx |+,J,\tau\rangle + \sum_{\tau'}|-,J,\tau'\rangle\frac{V^{-+}_{J\tau' J\tau}}{E^{+}_{J\tau} - E^{-}_{J\tau'}} \equiv |+,J,\tau\rangle + \sum_{\tau'} c^{+-}_{J\tau J\tau'}|-,J,\tau'\rangle \quad (14a)$$

$$|(-,J,\tau)\rangle \approx |-,J,\tau\rangle + \sum_{\tau'}|+,J,\tau'\rangle\frac{V^{+-}_{J\tau' J\tau}}{E^{-}_{J\tau} - E^{+}_{J\tau'}} \equiv |-,J,\tau\rangle + \sum_{\tau'} c^{-+}_{J\tau J\tau'}|+,J,\tau'\rangle \quad (14b)$$

Replacing the above wave functions in eqs 10 and carrying out some tedious but straightforward algebra gives

$$\mu^{\pm\pm}_{J,\tau,M,J',\tau',M} \approx \langle\mu_b\rangle\phi^{b}_{J\tau MJ'\tau' M} + \langle\mu_a\rangle[\sum_{\tau''}(c^{\pm\mp}_{J,\tau,J,\tau''})^*\phi^{a}_{J\tau'' MJ'\tau' M} + \sum_{\tau'''} c^{\pm\mp}_{J',\tau',J',\tau'''}\phi^{a}_{J\tau MJ'\tau''' M}] \quad (15a)$$

$$\mu^{\pm\mp}_{J,\tau,M,J',\tau',M} \approx \langle\mu_a\rangle\phi^{a}_{J\tau MJ'\tau' M} + \langle\mu_b\rangle[\sum_{\tau''}(c^{\pm\mp}_{J,\tau,J,\tau''})^*\phi^{b}_{J\tau'' MJ'\tau' M} + \sum_{\tau'''} c^{\mp\pm}_{J',\tau',J',\tau'''}\phi^{b}_{J\tau MJ'\tau''' M}] \quad (15b)$$

This modifies the simplified picture given earlier and, in particular, introduces *both* $\langle\mu_a\rangle_v$ and $\langle\mu_b\rangle_v$, dependence into each dipole moment matrix element, causing interference between the two terms. This interference, which can be constructive or destructive, mostly affects the $\mu^{\pm\mp}_{J,\tau,M,J',\tau',M}$ dipole matrix elements, on account of the large ratio of $\langle\mu_b\rangle_v$ to $\langle\mu_a\rangle_v$.

Hence, the inertial axes tilt $\rho$ has two important consequences:

(1) it gives the dominant contribution to the nonzero $\mu_a$ component in the local-mode picture discussed earlier, and

(2) it is responsible for the partial scrambling of $\mu_a$ and $\mu_b$ contribution to dipole moment matrix elements.

The perturbational approach presented so far provides a very good understanding of the underlying physics, and a clear link between the measured Stark coefficients $C_i$ and the relevant molecular properties $\langle\mu^g\rangle_v$. In fact, the combined experimental data available are sufficient to extract reasonably accurate values for $\langle\mu_a\rangle_v$ and $\langle\mu_b\rangle_v$ from the experimental Stark coefficients using eqs 4 and 10 or eqs 4 and 15. Specifically, the energies $E_i$ of the relevant states are known[34] to an accuracy of a few thousandths of a $cm^{-1}$, the $\phi^{g}_{J\tau MJ'\tau' M}$ direction cosine matrix elements can be determined with sufficient accuracy, and the $c^{\pm\pm}_{J\tau J'\tau'}$, $c^{\pm\mp}_{J\tau J'\tau'}$ coefficients can also be determined (with lesser accuracy, but still sufficient, because of their smaller contribution). However, this approach has two drawbacks. First, it is computationally cumbersome; second, and most important, it provides only the dipole moment components in the rotated $a-b$ frame, and not in the fixed $z-x$ frame. Hence, it does not provide enough information to disentangle the contribution of nuclear mass displacement (frame rotation, $\rho$) from electric charge redistribution (dipole rotation, $\eta$).

**D. Numerical Diagonalization and Model.** We have used numerical diagonalization of eq 8 to tackle both the drawbacks mentioned above. On one hand, the powerful suite of programs SPFIT/SPCAT[36,37] makes the task much more practical and straightforward. On the other hand, fitting the Hamiltonian to accurately known ro-vibrational energy levels should, in principle, provide all the relevant parameters, including the tilt of inertial axes $\rho$. For this, it is convenient to rewrite the Hamiltonian with the angular momentum operators referred to the $C_{2v}$ inertial axis system. Following Lehmann,[35] we write

$$\begin{aligned}\mathbf{H} = {} & [G_0 + \lambda + A_+\hat{J}_z^2 + B_+\hat{J}_x^2 + C_+\hat{J}_y^2]|+\rangle\langle+| + \\ & [G_0 - \lambda + A_-\hat{J}_z^2 + B_-\hat{J}_x^2 + C_-\hat{J}_y^2]|-\rangle\langle-| + \\ & \frac{1}{2}d_{+-}\{\hat{J}_x,\hat{J}_y\}[|+\rangle\langle-| + |-\rangle\langle+|]\end{aligned} \quad (16)$$

with

$$\begin{aligned} A_+ &= A_- = A\cos^2\rho + B\sin^2\rho \\ B_+ &= B_- = A\sin^2\rho + B\cos^2\rho \\ C_+ &= C_- = C \\ d_{+-} &= (A - B)\sin(2\rho) \end{aligned} \quad (17)$$

and

$$|+\rangle \equiv \frac{|1\rangle + |2\rangle}{\sqrt{2}} \quad (18a)$$

$$|-\rangle \equiv \frac{|1\rangle - |2\rangle}{\sqrt{2}} \tag{18b}$$

We notice, in passing, that without the inertial axes tilt ($\rho = 0$), we would have $d_{+-} = 0$; hence, the Hamiltonian written in eq 16 could be separated into two standard rigid rotor Hamiltonians, with vibrational eigenstates $|+\rangle$ and $|-\rangle$, but this is no longer possible when $d_{+-} \neq 0$, since the corresponding term scrambles the ro-vibrational states inextricably.

In principle, it is possible, from a fit to the experimental energy levels, to extract $d_{+-}$ and, hence, $\rho$. In practice, unfortunately, this was not possible because the value of $d_{+-}$ is much too sensitive to the many small perturbations inevitably present at these highly excited energy levels. Attempts to use this approach resulted in poor convergence of the fit, with values of $d_{+-}$ that strongly depended on the rotational states included in the fit and that were often unrealistic. Therefore, to get a better estimate of the inertial axes tilt, and disentangle the various contributions to the dipole moment vibrational dependence, we have used a semiempirical model, similar to the one we have used to model the dipole moment vibrational dependence in HDO.[19] Briefly, the model calculates vibrationally averaged molecular properties by treating the excited bond as a quantum-mechanical Morse oscillator, while keeping the unexcited bond and the bending angle fixed.

Specifically, we define the $|n,0\rangle$, or $|1\rangle$, basis state of $H_2O$ by using a Morse oscillator (having $\alpha = 2.14$ Å$^{-1}$ and $D = 47\,500$ cm$^{-1}$) to describe the vibrationally excited O−H bond 1, while O−H bond 2 is fixed at the ground state value of $R_2 = 0.9724$ Å.[38] The molecular description is completed by selecting a fixed value for the bond angle, $\theta$, which will be later adjusted iteratively to the value of $\theta$ that gives the best agreement between calculated and observed $1_{01}$, $1_{11}$, and $1_{10}$ rotational energy levels.

At each point on the Morse oscillator trajectory along the O−H bond 1, the $H_2O$ center of mass is placed at the origin of a coordinate system having one axis parallel to the bond angle bisector and, relative to this frame, we define an $z-x$ "Eckart bisector frame" as described by Wei and Carrington.[39,40] Using the same procedures we implemented for HDO, we calculate the vibrationally averaged kinetic energy operators, $\langle G_{xx}\rangle_v$, $\langle G_{yy}\rangle_v$, $\langle G_{zz}\rangle_v$, $\langle G_{xz}\rangle_v$ by numerical integration over the vibrational trajectory of the corresponding operators, weighted by the Morse oscillator probability density.

Diagonalization of this vibrationally averaged Hamiltonian provides rotational energies, the usual $A$, $B$, and $C$ rotational constants, and the angle $\rho$ between the $a-b$ inertial axes and the $z-x$ axes:[39,40]

$$\rho_v = \frac{1}{2}\arctan\frac{2\langle G_{xz}\rangle_v}{\langle G_{xx}\rangle_v - \langle G_{zz}\rangle_v} \tag{19}$$

We repeat this averaging procedure, treating the bond angle, $\theta$, as a parameter that is adjusted iteratively to the value that gives the best agreement between calculated and observed $1_{01}$, $1_{11}$, and $1_{10}$ rotational energy levels. In this way we obtain the $A$, $B$, and $C$ rotational constants, the optimum bond angles, $\theta_v$, and the inertial-axes rotation $\rho_v$, for the $|4,0\rangle$, $|4,0\rangle|2\rangle$, $|5,0\rangle$, and $|8,0\rangle$ basis states.[41] These values are listed in Table 3.

With the molecular geometries defined in this way for each vibrational state, we calculate the dipole moment components in the $z-x$ Eckart bisector frame at each point along the $R_1$ vibrational trajectory from the revised DMS of Schwenke and Partridge.[42] The vibrational average of these components, $\langle\mu_x\rangle_v$ and $\langle\mu_z\rangle_v$, are then projected onto the $a-b$ inertial axes to obtain $\langle\mu_a\rangle_v$ and $\langle\mu_b\rangle_v$ values.

**TABLE 3: Parameters of the One-Dimensional Morse Oscillator Model[a]**

| $\|n,0^{\pm}\rangle\|b\rangle$ | $\theta_v$ | $G_{zz}/2$ | $G_{xx}/2$ | $G_{yy}/2$ | $G_{xz}/2$ | $A$ | $B$ | $C$ | $\rho$ |
|---|---|---|---|---|---|---|---|---|---|
| $\|4,0^-\rangle$ | 104.19 | 24.83 | 13.33 | 8.36 | −1.14 | 24.94 | 13.22 | 8.36 | 5.60 |
| $\|4,0^-\rangle\|2\rangle$ | 114.64 | 32.13 | 11.71 | 8.28 | −1.20 | 32.20 | 11.64 | 8.28 | 3.36 |
| $\|5,0^-\rangle$ | 105.63 | 25.19 | 12.83 | 8.11 | −1.47 | 25.36 | 12.65 | 8.11 | 6.70 |
| $\|8,0^+\rangle$ | 101.21 | 21.55 | 12.83 | 7.41 | −2.45 | 22.19 | 12.19 | 7.41 | 14.65 |

[a] Rotational constants are given in units of cm$^{-1}$, and angles, in degrees.

We then use these rotational constants and dipole moments as input to the SPFIT/SPCAT programs to calculate all the necessary dipole moment matrix elements, and from these, the Stark coefficients, which we compare with our experimental measurements. In addition, it is possible, just by changing the input parameters to SPFIT/SPCAT, to recalculate the same Stark coefficients at various levels of approximation, corresponding to first- and second-order of perturbation, and also to separate the contribution of $b$-type dipole matrix elements (vertical lines in Figure 4) from that of $a$-type dipole matrix elements (diagonal lines in Figure 4). All of these results are listed in Table 4. It can be seen from this table that this simple model nicely captures the complex dependence of the dipole moment upon vibrational state, and we can reproduce within few percents the experimental Stark coefficients, and thus the dipole moment matrix elements.

Finally, the rotational constants in Table 3 are used with SPFIT/SPCAT to find the values of $\mu_a$ and $\mu_b$ (hence, $\mu_z$ and $\mu_x$) that give the best agreement with the experimentally observed Stark coefficients. These values are listed in Table 5 and compared with the values derived above from DMS.

## IV. Discussion

Tables 4 and 5 summarize the core results of our analysis. The data they contain can be read in several different ways, depending on what is being compared with what (for example, one can compare the results of a given model for different vibrational states, or the results of different models for the same vibrational state, and so on). Each way of comparing provides interesting and somewhat complementary information, and we will focus on a number of them, in turn.

Starting with the results of the exact diagonalization of our model Hamiltonian (panel I of Table 4), we can see that the calculated value for the Stark coefficients is in most cases within a few percent of the experimental value. One obvious exception is the $|40^-\rangle|2\rangle$ state, which we take as an indication that keeping the HOH angle fixed at an average value (as we do in our simple model) cannot fully account for the presence of bending motion. The other main exceptions are found for those Stark coefficients that have a substantial contribution from $a$-type dipole moment matrix elements (i.e., from the $\mu^{\pm\mp}_{J,\tau,M,J',\tau',M}$ represented as diagonal lines across the two vibrational manifolds in Figure 4). The reason why these particular contributions are comparatively large is that energy separation between the two states involved is particularly small (less than a few cm$^{-1}$); hence, the small denominator in eq 4 amplifies the corresponding contribution to the Stark coefficient. This is clearly visible in Figure 4, where the $|40^-\rangle|1_{11}\rangle$ and the $|40^+\rangle|1_{10}\rangle$ are very close in energy to one another, compared with the typical separation between the other energy levels. The most striking example comes from the $|40^-\rangle|2\rangle|1_{10}\rangle$ state, which is accidentally nearly degenerate with

**TABLE 4: Comparison of Experimental Water Stark Coefficients with Calculations at Different Levels of Approximation[a]**

| | | | calculated % contribution | | | | | | | | |
|---|---|---|---|---|---|---|---|---|---|---|---|
| | | | I. full | | | II. first order | | | III. no tilt | | |
| $\|n,0^{\pm}\rangle\|b\rangle$ | $J_{K_aK_c}$ | $C_{exp}$ | tot | *b*-type | *a*-type | tot | *b*-type | *a*-type | tot | *b*-type | *a*-type |
| $\|4,0^-\rangle$ | $1_{01}$ | 0.4372(8) | 99.1 | 97.0 | 2.1 | 99.2 | 97.9 | 1.3 | 99.5 | 99.4 | 0.1 |
| | $1_{11}$ | 0.3160(9) | 93.5 | 82.3 | 11.2 | 97.3 | 81.6 | 15.7 | 83.6 | 82.8 | 0.9 |
| | $1_{10}$ | 0.5097(10) | 97.2 | 92.5 | 4.7 | 96.4 | 93.2 | 3.2 | 94.8 | 94.7 | 0.2 |
| $\|4,0^-\rangle\|2\rangle$ | $1_{01}$ | 0.3153(26) | 86.7 | 85.6 | 1.2 | 86.8 | 85.4 | 1.4 | 86.5 | 86.2 | 0.3 |
| | $1_{11}$ | 0.2137(39) | 90.9 | 87.7 | 3.2 | 90.7 | 87.9 | 2.8 | 89.2 | 88.6 | 0.6 |
| | $1_{10}$ | 0.6306(27) | 63.1 | −48.4 | 111.5 | 74.0 | −48.3 | 122.4 | −23.3 | −48.8 | 25.5 |
| $\|5,0^-\rangle$ | $1_{01}$ | 0.4277(7) | 96.6 | 94.4 | 2.2 | 96.6 | 94.5 | 2.1 | 96.8 | 96.6 | 0.1 |
| | $1_{11}$ | 0.3032(7) | 93.0 | 82.1 | 11.0 | 93.4 | 81.9 | 11.4 | 84.3 | 83.7 | 0.6 |
| | $1_{10}$ | 0.5077(4) | 94.9 | 88.4 | 6.5 | 94.8 | 88.5 | 6.3 | 90.8 | 90.5 | 0.4 |
| $\|8,0^+\rangle$ | $1_{01}$ | 0.4953(16) | 100.2 | 93.6 | 6.6 | 100.2 | 93.6 | 6.6 | 101.0 | 100.9 | 0.0 |
| | $1_{11}$ | 0.4250(10) | 92.5 | 64.5 | 28.0 | 92.5 | 64.5 | 28.0 | 69.3 | 69.2 | 0.1 |
| | $1_{10}$ | 0.6657(38) | 96.7 | 77.8 | 18.8 | 96.7 | 77.8 | 18.8 | 84.0 | 83.9 | 0.1 |

[a] The calculated Stark coefficients are expressed as % of the experimental value; the contribution of dipole moment matrix elements with *a*-symmetry and *b*-symmetry is also listed separately. Full: exact diagonalization of the model Hamiltonian. First order ($\lambda \sim 0$): only $\Delta\tau = 0$ coupling from $\lambda$ $[|1\rangle\langle 2| + |2\rangle\langle 1|]$. No tilt ($d_{+-} \sim 0$): neglecting the tilt of inertial axis upon local mode stretching.

**TABLE 5: Comparison between Dipole Moments Derived from Dipole Moment Surface (DMS) and from Experimentally Measured Stark Coefficients**

| $\|n,0^{\pm}\rangle\|b\rangle$ | | $\mu_z$ | $\mu_x$ | $\mu_a$ | $\mu_b$ | $\mu_{tot}$ |
|---|---|---|---|---|---|---|
| $\|4,0^-\rangle$ | DMS | −0.057 | +1.882 | −0.240 | +1.867 | +1.882 |
| | Stark | −0.102 | +1.895 | −0.287 | +1.876 | +1.898 |
| $\|4,0^-\rangle\|2\rangle$ | DMS | −0.084 | +1.711 | −0.184 | +1.704 | +1.714 |
| | Stark | −0.110 | +1.821 | −0.216 | +1.811 | +1.824 |
| $\|5,0^-\rangle$ | DMS | −0.067 | +1.856 | −0.283 | +1.835 | +1.857 |
| | Stark | −0.119 | +1.886 | −0.338 | +1.859 | +1.889 |
| $\|8,0^+\rangle$ | DMS | −0.034 | +1.890 | −0.511 | +1.820 | +1.890 |
| | Stark | −0.111 | +1.885 | −0.585 | +1.796 | +1.889 |

the $|40^+\rangle|1_{11}\rangle$, resulting in an anomalously large *a*-type contribution. While, at first sight, this might seem a problem, it is, on the contrary, an excellent opportunity to sort out the contribution of the *a*-type dipole moment matrix elements, which would otherwise be "buried" in the much larger *b*-type contribution.

Furthermore, comparing the results of panel I (full model) with those of panel III (no tilt), it becomes immediately clear that most of the *a*-type contribution is due to the tilt of inertial axes, which is a purely "mechanical" effect, and only a minor part from the change of electric charge distribution within the molecule, which is the dominant contribution for most other molecules. Considering the good agreement obtained for the Stark coefficients that do not have a substantial *a*-type contribution, we conclude that (a) the level of accuracy of the DMS used is certainly a very good one, and probably better than our simple model can probe; (b) most of the current uncertainty comes from "mechanical" effects and the associated difficulties in calculating sufficiently accurate molecular wave functions.

We note, in passing, that this kind of analysis has allowed us to identify the main source of the disagreement previously reported[16] between the results of experimental measurements and of direct ab initio calculations of the $C_i$, with the calculations giving Stark coefficients that differed by up to 10% from the measurements. In the course of the present work it was found that the majority of this discrepancy was caused by the use of an incorrect (Eckart) embedding of the body-fixed axis system.[43] This embedding is close to, but not the same as, the bisector embedding[44] used to compute the wave functions, and the use of the correct embedding has significantly reduced these errors.[17]

Continuing our comparison between the panels of Table 4, we see that the results of the first-order approximation are fairly close to those obtained by exact diagonalization of our model Hamiltonian. This, in turn, indicates that describing water's eigenstates as being the symmetric and antisymmetric combination of two local mode states with the same rotational quantum numbers, but referred to different inertial axes (eq 9), is indeed a very good approximation of the true eigenstates, and that the additional mixing occurring when the time scale of tunneling and of rotational motion is comparable results only in a small correction. It is not surprising that this correction becomes smaller and smaller as we go to higher vibrational states, since the local mode coupling responsible for tunneling becomes smaller (i.e., the tunneling time becomes longer, and the local-mode approximation, better).

Having established a reasonable level of confidence in our semiempirical model, we now use it do discuss the evolution of the dipole moment upon vibrational excitation. For this we turn to Table 5, with the dipole moments and their projection on the molecule-fixed bisectrix reference frame and the inertia-axes reference frame. Results labeled as (DMS) are those obtained using known measured energies as the only experimental input data and deriving everything else from our model, using the DMS of Partridge and Schwenke. Results labeled as (Stark) are those obtained when $\mu_a$ and $\mu_b$ are instead adjusted to obtain the best agreement with experimental Stark coefficients. The latter procedure is somewhat analogous to the traditional dipole moment analysis, except for the way rotational constants (and wave functions) are derived from experimental energy levels (Table 3). It is important to point out that the largest uncertainty in these two procedures comes from the difficulty of deriving an accurate value for the tilt of the inertia frame ($\rho$). This uncertainty affects the accuracy of the results reported in Table 5 in different ways. The dipole moments projection derived from DMS are calculated first in the $z-x$ frame, and then referred to the $a-b$ frame; hence, for these the $\mu_z$ and $\mu_x$ values are the most accurate. Conversely, the experimental Stark coefficients are related first to $\mu_a$ and $\mu_b$, and then to $\mu_z$ and $\mu_x$, through the rotation of the reference frame; hence, for these the $\mu_a$ and $\mu_b$ values are the most accurate. In both cases, the total dipole is independent of the frame rotation and the corresponding values can be compared across the two sets, providing an indication of the accuracy of the DMS. With one exception, the values of $\mu_{tot}$ derived from DMS agree to within a few percent with those derived from experimental Stark coefficients, thus confirming the substantial accuracy of the DMS. The exception occurs for the $|40^-\rangle|2\rangle$ where the dipole

value derived from the DMS is substantially lower than the value from experimental data. This again indicates that the effects of vibrational bending excitation cannot be accurately lumped into an effective bending angle. A more accurate approach would be to treat the bending coordinate also as a quantum mechanical oscillator, i.e., "upgrading" to a two-dimensional quantum oscillator model. This would likely give new and important insight into the role of bending motion, at the price, however, of an inevitable increase in the model complexity.

It should be pointed out that this kind of simplified approach cannot substitute for high-level, full quantum mechanical calculations and for the level of accuracy they can afford, when it comes to giving the DMS the ultimate test against experimentally measured Stark coefficients. However, simplified models can (and should) complement high-level calculations by providing the precious insight that is otherwise buried in the complexity of these difficult and computationally intensive calculations. Finally, we notice that the vibrational evolution of dipole moments is dominated by "mechanical effects" (i.e., tilt of the reference frame), and that the contribution of charge redistribution within the molecule is quite small, in comparison. Hence, future high-level calculations would have to focus as much on getting these mechanical effects right as on calculating an accurate dipole moment surface.

In conclusion, we have presented here a detailed analysis of Stark induced quantum beats measured in highly excited vibrational states of water. These measurements, which extend to states having more than half of the O−H bond dissociation energy, provide exceptional detail on how the electronic structure of water changes upon excitation of the O−H bond. The perturbation theory based model we have used gives considerable insight into the complex effects of energy tunneling between the two identical O−H bonds, and it clearly shows how these must be accounted for when analyzing the Stark effect and deriving permanent dipole moment components of water. The accurate Stark coefficients and dipole moment components, and the analysis presented here will serve as important benchmarks for future potential energy and dipole moment surfaces of water. Improved confidence in theoretical calculations should lead to a better understanding of water's role in energy transfer processes in the Earth's atmosphere and improve quantitative modeling of the greenhouse effect. Finally, the experimental methods employed in this work are quite general and can be used to extend electric dipole moment measurements to much higher energies for a wide variety of molecules.

**Acknowledgment.** This work was supported by the Swiss Science Foundation, and the European Community (SPHERS program). J.S.M. thanks Tom Rizzo and all the members of the LCPM for making his visits to EPFL both pleasant and productive.

## References and Notes

(1) Ramanathan, V.; Vogelmann, A. M. *Ambio* **1997**, *26*, 38.
(2) Wayne, R. P. *Chemistry of Atmospheres*, 3rd ed.; Oxford University Press, New York; 2000.
(3) Belmiloud, D.; Schermaul, R.; Smith, K. S.; Zobov, N. F.; Brault, J. W.; Learner, R. C. M.; Newnham, D. A.; Tennyson, J. *Geophys. Res. Lett.* **2000**, *27*, 3703.
(4) Mlawer, E. J.; Brown, P.; Clough, S.; Harrison, L.; Michalsky, J.; Kiedron, P.; Shippert, T. *Geophys. Res. Lett.* **2000**, *27*, 2653.
(5) Arking, A. *Geophys. Res. Lett.* **1999**, *26*, 2729.
(6) Arking, A. *Science* **1996**, *273*, 779.
(7) Bernath, P. F. *Phys. Chem. Chem. Phys.* **2002**, *4*, 1501.
(8) Halkier, A.; Klopper, W.; Helgaker, T.; Jorgensen, P. *J. Chem. Phys.* **1999**, *111*, 4424.
(9) de Oliveire, G.; Dykstra, C. E. *Theor. Chem. Acc.* **1999**, *11*, 435.
(10) Kjaergaard, H. G.; Bezar, K. J.; Brooking, K. A. *Mol. Phys.* **1999**, *96*, 1125.
(11) Townes, C. H.; Schawlow, A. L. *Microwave Spectroscopy*; McGraw-Hill, New York: 1955.
(12) Dyke, T. R.; Muenter, J. S. *J. Chem. Phys.* **1973**, *59*, 3125.
(13) Shostak, S. L.; Ebenstein, W. L.; Muenter, J. S. *J. Chem. Phys.* **1991**, *94*, 5875.
(14) Shostak, S. L.; Muenter, J. S. *J. Chem. Phys.* **1991**, *94*, 5883.
(15) Mengel, M.; Jensen, P. *J. Mol. Spectrosc.* **1995**, *169*, 73.
(16) Callegari, A.; Theule, P.; Muenter, J. S.; Tolchenov, R. N.; Zobov, N.; Polyanski, O.; Tennyson, J.; Rizzo, T. R. *Science* **2002**, *297*, 993.
(17) Theule, P. Electric dipole moment of highly excited molecular vibrational states, Thesis, Ecole Polytechnique Federale de Lausanne (EPFL), 2003.
(18) Theule, P.; Callegari, A.; Rizzo, T. R.; Muenter, J. S. *J. Chem. Phys.* **2003**, *119*, 8910.
(19) Theule, P.; Callegari, A.; Rizzo, T. R.; Muenter, J. S. *J. Chem. Phys.* **2005**, *122*, 124312.
(20) Muenter, J. S. In *Atomic and Molecular Beam Methods*; Vol. II; Scoles, G., Ed.; Oxford University Press: London: 1992; Vol. II, Chapter 2, pp 15−57.
(21) Vaccaro, P. H.; Kinsey, J. L.; Dai, H.-L.; Field, R. W. *J. Chem. Phys.* **1983**, *78*, 3659.
(22) Vaccaro, P. H.; Zabludoff, A.; Carrera-Patino, M. E.; Kinsey, J. L.; Field, R. W. *J. Chem. Phys.* **1989**, *90*, 4150.
(23) Bitto, H.; Huber, J. R. *Opt. Commun.* **1990**, *80*, 184.
(24) Schmidt, P.; Bitto, H.; Huber, J. R. *J. Chem. Phys.* **1988**, *88*, 696.
(25) Child, M. S.; Lawton, R. T. *Chem. Phys. Lett.* **1982**, *87*, 217.
(26) Another commonly used labeling scheme for the vibrational states of water is based on the normal mode notation ($\nu_1\nu_2\nu_3$). The correlation between local mode and normal mode notation for the states we studied is given here for completeness: $|4,0^-\rangle \leftrightarrow (301)$; $|4,0^-\rangle|2\rangle \leftrightarrow (321)$; $|5,0^-\rangle \leftrightarrow (401)$; $|8,0^+\rangle \leftrightarrow (800)$.
(27) Barnes, R. J.; Gross, A. F.; Sinha, A. *J. Chem. Phys.* **1997**, *106*, 1284.
(28) Vanderwal, R. L.; Scott, J. L.; Crim, F. F. *J. Chem. Phys.* **1991**, *94*, 1859.
(29) Zare, R. N. *Angular Momentum*; Wiley: New York: 1988.
(30) Child, M. S.; Halonen, L. *Adv. Chem. Phys.* **1984**, *57*, 1.
(31) Child, M. S.; Lawton, R. T. *Faraday Discuss. Chem. Soc.* **1981**, *71*, 273.
(32) Mandin, J. Y.; Chevillard, J. P.; Camy-Peyret, C.; Flaud, J. M.; Brault, J. *J. Mol. Spectrosc.* **1986**, *116*, 167.
(33) Camy-Peyret, C.; Flaud, J.-M.; Mandin, J.-Y.; Chevillard, J.-P.; Brault, J.; Ramsay, D. A.; Vervloet, M.; Chauville, J. *J. Mol. Spectrosc.* **1985**, *113*, 208.
(34) http://www.tampa.phys.ucl.ac.uk/ftp/astrodata/water/levels/.
(35) Lehmann, K. K. *J. Chem. Phys.* **1991**, *95*, 2361.
(36) Pickett, H. M. *J. Mol. Spectrosc.* **1991**, *148*, 371–377.
(37) http://spec.jpl.nasa.gov/ftp/pub/calpgm/.
(38) Cook, R. L.; Lucia, F. C. D.; Helminger, P. *J. Mol. Spectrosc.* **1974**, *53*, 62.
(39) Wei, H.; Carrington, T. *J. Chem. Phys.* **1997**, *107*, 2813.
(40) Wei, H.; Carrington, T. *J. Chem. Phys.* **1997**, *107*, 9493.
(41) Alternatively, the relevant rotational constants can be extrapolated from the accurately known constants of the ground- and first excited- states. This gives fairly good results for $G_{xc}/2$: respectively 1.28, 1.28, 1.59, and 2.55 for $|40^-\rangle$, $|40^-2\rangle$, $|50^-\rangle$, and $|80^+\rangle$. The results for {*A*, *B*, *C*} are less satisfactory: respectively, {23.90, 13.91, 8.65}, {31.60, 14.23, 8.35}, {22.90, 13.75, 8.50}, and {19.92, 13.29, 8.03}.
(42) Schwenke, D. W.; Partridge, H. *J. Chem. Phys.* **2000**, *113*, 6592.
(43) Lesueur, C. R.; Miller, S.; Tennyson, J.; Sutcliffe, B. *Mol. Phys.* **1992**, *76*, 1147.
(44) Tennyson, J.; Sutcliffe, B. T. *Int. J. Quantum Chem.* **1992**, *42*, 941.

JP904035G